1 **Characterisation of porous anodic alumina membranes for ultrafiltration of**

2 **protein nanoparticles as a size mimic of virus particles**

3 Anshul Sharma [a], Daniel G. Bracewell [a]*

4 [a] Department of Biochemical Engineering, Gower Street, University College London, UK WC1E 6BT

5 *Corresponding author (Email: d.bracewell@ucl.ac.uk)

6 **Declarations of Interest:** none

7 **Keywords**

9 **Abstract**

10 Viral vectors used in emerging gene therapies face challenges of significant yield loss during

11 downstream processing primarily due to their large size, fragility and mass transfer limitations of the

12 traditional porous chromatography adsorbents. The large size of the vectors in relation to key

13 impurities makes them suitable solutes for ultrafiltration-based separations. Efforts to utilise

14 ultrafiltration for virus purification are often restricted to commercial polymeric membranes with wide

15 pore size distributions and tortuous, interconnected channels. Membranes with narrow pore

16 distributions and straight pore channels such as porous anodic alumina (PAA) may present

17 opportunities for improved virus purification. This paper examines the use of porous anodic alumina

18 membranes for application in virus separation by using model solutes such as thyroglobulin and

19 protein nanoparticles. A systematic approach is used to select a polymeric ultrafiltration membrane

20 rating for comparison with 20nm rated PAA membrane by comparing hydraulic permeability and

21 dextran sieving characteristics of the membranes. Differences in the filterability of the model solutes

22 were characterised. Finally, a discontinuous diafiltration experiment was employed to fractionate

23 smaller model impurity and protein nanoparticles. Results indicate that PAA membranes have

24 superior fouling resistance with 3-4 folds higher flux recovery ratio and 3-fold higher purification

25 factors compared to the polymeric membranes, but the presence of surface defects make them more

26 susceptible to product loss through leaky transmission.

27 **1. Introduction**

28 Emerging therapies such as gene therapy and cell therapies employ viral vectors for vaccine and

29 therapeutic uses. Biomanufacturing of the viral vectors at present suffers from low process yields due

30 to suboptimal chromatography processes due to inaccessibility of the resin pores for large solutes

31 such as viral vectors resulting in an order of magnitude lower binding capacities compared to proteins

32 [1]. New materials with a more open porous architecture such as gigaporous resins [2], monoliths [3,

33 4] and nanofiber adsorbers [5] are being actively looked into. Limited studies have been carried out to

34 explore the use of ultrafiltration based processing instead of chromatography based processes by

1

exploiting differences in the size of impurities and viral particles [6-9]. Most of the reported literature compares different molecular weight rating or pore size ratings of polymeric ultrafiltration membranes or different modules such as hollow fibre and cassette [6, 8]. These membranes have wide pore size distribution, which is often reported to affect the membrane performance especially retention of large biomolecules such as viruses [10, 11]. Isoporous membranes with different porous architectures such as porous anodic alumina (PAA) membranes are however being investigated in other fields such as nanofiltration for water purification and biosensors.

Porous anodic alumina membranes are widely studied for applications in label-free biosensors [12-14] for use as point-of-care diagnostic devices. Applications of PAA membranes in bioseparations have been limited to diffusion based separations for haemodialysis [15], separation of similarly sized proteins by exploiting differences in solute charge [16], enriching phosphoproteins for mass spectrometry [17] and ultrafiltration of small proteins [18-20]. A few reports on PAA membranes have examined their potential for virus separations. Moon et al., [21] reported the ability of 35-nm pores of a PAA membrane to separate empty and genome filled virus particles of a bacteriophage in centrifugal filtration. Jeon et al., [22] have described the use of a PAA membrane for enrichment of hepatitis C viruses and when compared to ultracentrifugation achieved four times higher recovery. These studies, however, did not compare the PAA membranes to conventionally used polymeric membranes and also did not study filtration performance such as flux decline and fouling of the membranes. Further, most of the studies have used custom fabricated membranes and not the commercially available membranes. This work evaluates a commercial PAA membrane for filtration and separation performance and compares them with a traditional polymeric membrane for potential applications in virus ultrafiltration.

Working with live virus feeds can be challenging due to laborious, time and resource consuming cell culture-based production and subsequent recovery of labile virus particles, the requirement for biosafety containment for all of the experiments and sophisticated analytical tools required such as infectivity and immunochemical assays. Nano-particulates such as inclusion bodies [23] and synthesised protein nanoparticles [24] have been previously used in purification studies as surrogates for virus particles. In this article, we report on the use of model solutes such as large proteins and protein nanoparticles as mimics for viral vectors in ultrafiltration studies. Monodisperse bovine serum albumin nanoparticles (BSA NP) preparations were prepared as reported in the literature [25]. This paper presents a systematic approach for the selection of pore ratings for porous anodic alumina and polymeric membranes to compare these two membrane types of radically different architecture for filterability of large biomolecules. BSA NP of 80-90 nm diameter and thyroglobulin of 20 nm diameters are used as physical mimics for viral vectors representing larger adenovirus and smaller vectors, such as adeno-associated virus respectively. Bovine serum albumin of 66 kDa is used as a model impurity given that most of the host cell proteins in mammalian cell cultures are in the range of 50-100 kDa in molecular weight [26] and albumin is also the most abundant protein in the serum supplemented growth media used in mammalian cell culture. Membrane fouling by these large solutes is studied, and mechanisms of fouling are identified using a statistical curve fitting of experimental data with

74 established mathematical models [27]. Separation performance of the membranes was also

75 compared using mixtures of the model solutes and impurity (BSA) and performing an ultrafiltration-

76 diafiltration (UF/DF) run to aid in the fractionation. A hypothesis is put forward to explain the

77 differences observed in fouling and sieving behaviour of the two membranes on the basis of

78 differences in their architecture.

79 **2. Materials and methods**

80 Filtration experiments were carried out in a 25 mm diameter Amicon stirred cell from EMD Millipore,

81 USA using 25 mm diameter membrane discs. Commercial PAA membranes with 20 nm pore rating

82 (Whatman® Anodisc™ 25, GE Healthcare, UK) and three polyethersulfone (PES) ultrafiltration

83 membranes (Biomax®, EMD Millipore, USA) of 100, 300 and 500 kDa ratings (as rated by the

84 manufacturer) were used. PAA membranes had a 3 mm wide polypropylene support ring hence

85 reducing the effective diameter to 19 mm. Bovine serum albumin (BSA) and bovine thyroglobulin (TG)

86 were obtained from Sigma-Aldrich, USA. Protein nanoparticles were synthesised from BSA as

87 mentioned below in section 2.1. BSA, TG and BSA NP were used as model protein solutes. Feed

88 solutions of BSA, TG and BSA NP were prepared in phosphate buffer saline at pH 7.4 with respective

89 concentrations of 1.0, 0.2 and 1.0 mg/mL as measured using absorbance at 280 nm wavelength. TG

90 at 0.2 mg/mL corresponded to approximately 10^{18} particles/mL as estimated from molecular weight of

91 the TG and Avogadro's number. For BSA NP, 1.0 mg/mL concentration corresponded to a particle

92 titre of 1-3 x 10^{11} particles/mL as measured using nanoparticle tracking analysis (Nanosight LM-10,

93 Malvern Panalytical, UK). Powders of monodisperse GPC-standard dextrans (5, 12, 25, 50, 80, 120,

94 250, 450 and 660 kDa) and polydisperse dextrans (6, 40, 450 and 2000 kDa) were obtained from

95 Sigma-Aldrich, USA and Denmark respectively. Size exlusion columns, TSKgel3000SWXL and

96 TSKgel5000PWXL were obtained from Tosho Biosciences GmBH, Germany. Size exclusion column,

97 BioSEC-5 was obtained from Agilent,USA.

98 **2.1 Preparation of BSA nanoparticles**

99 A protocol for albumin nanoparticle synthesis was adopted from Storp et al.[25] and modified for use

100 with bovine serum albumin in a shorter preparation time of 4 hours. BSA solution of 100 g/L was

101 prepared in 10mM NaCl solution and the pH of the solution was adjusted to 8.0 using 1M NaOH and

102 subsequently filtered through a 0.22 μm PES syringe filter. BSA solution (1 mL) was precipitated by

103 addition of a desolvating mixture (~2-3 mL) of methanol and ethanol in the ratio of 70:30 at a flow rate

104 of 1 mL/min while the protein solution was stirred at 550 rpm using a magnetic stirrer and bar. Glass

105 beaker of 25 mm diameter and 60 mm height and stirrer bar of 6mm diameter and 20 mm length were

106 used. Addition of the desolvating mixture was stopped as soon as protein solution turned turbid and

107 was then spiked with 60 μL of 8% (v/v) glutaraldehyde solution to cross-link the nanoparticles. Cross-

108 linking was carried out for 2 hours at room temperature at the same stirring conditions. At the end of

109 crosslinking, the nanoparticle preparation was diluted approximately 50-fold in the buffer solution and

110 analysed using dynamic light scattering for the particle size distribution.

2.2 Dextran sieving experiments

A mixture of four polydisperse dextrans in 20 mM phosphate buffer,pH 7.0 (with final concentrations of 1, 1, 1 and 0.5 mg/mL of 6, 40, 450 and 2000 kDa dextrans respectively) was filtered through membranes in a 25 mm stirred cell at constant filtrate flux of ~5.5 LMH (1.5-1.6 µm/s) using a peristaltic pump (120U, Watson Marlow) and a stirring rate of 1000 rpm. Approximately 20L/m^2 of the dextran feed was filtered and recirculated back to the stirred cell for two recirculation cycles as described in a similar protocol reported [28]. Final filtrate solution in the tubing and feed solution in the stirred cells were sampled and injected on to a size exclusion column, TSKgel5000PWXL (7.8 x 300 mm), pre-equilibrated with 20mM phosphate buffer at a flow rate of 0.3 mL/min. Refractive index detector, RID-20A (Shimadzu,UK) was used for detection of the dextran peaks. Calibration plot between peak elution volume and log value of the molecular weight of dextrans was obtained using injections of various monodisperse standard dextrans (5 to 660 kDa). Size exclusion chromatograms of the feed and filtrate samples were transformed by converting the elution volume into log molecular weight using the calibration equation. A continuous sieving curve was obtained by dividing the signals of filtrate with those of the feed at corresponding molecular weights from the transformed chromatograms.

2.3 Protein filtration experiments

PAA membranes were rinsed in 20% ethanol followed by pre-filtered and deionised water. PES membranes were rinsed thrice for 20 minutes using pre-filtered and deionised water as per manufacturer's instructions to remove any preservative. Initial buffer flux (J_o) was measured for clean membranes by filtering 20 L/m^2 of the pre-filtered buffer solution at the transmembrane pressure of 0.6 bar and a stirring rate of 1500 rpm. Equal membrane loadings (26.5 L/m^2) and conversion ratio (75%) or filtrate outputs (20 L/m^2) were used for both membranes. The transmembrane pressure of 0.6 bar was used for all protein filtration experiments. After filtration of protein solutions, retentate solution was carefully aspirated out. The membranes surface along with the stirred cell were rinsed three times with the buffer solution, and buffer flux was measured again in the same manner as for the initial buffer flux. Flux recovery ratio (FRR, %) was measured as a percentage of the initial buffer flux measured post filtration and rinsing. Filtrate, feed and retentate samples were collected and analysed for protein quantification using size exclusion chromatography as described in section 2.5. Recovery of the protein was calculated using the peak areas of the proteins in samples and feed solution and considering total volumes of the samples.

2.4 Fractionation experiment

A mixture of 80nm BSA nanoparticles and BSA was prepared in PBS with a final concentration of 1 mg/mL for both solutes. Fractionation was carried out in a sequential or discontinuous diafiltration mode after an initial concentration step. Equal membrane loadings of ~26 L/m^2 were applied on all the membranes and feed was initially concentrated 4-fold volumetrically. The retentate was then subjected to 12 diafiltration steps in sequence. Each diafiltration step involved a manual 2-fold dilution

148 of the retentate with PBS followed 2-fold concentration thus each diafiltration step corresponding to

149 one diavolume of the buffer exchanged. A transmembrane pressure of 0.6 bars and the maximum

150 stirring speed of 1500 rpm was used for the initial concentration step and subsequent diafiltration

151 steps. Filtrate collected for all steps of the UF/DF process and final retentate samples were analysed

152 for the model solutes using size exclusion chromatography as described in section 2.5. Purification

153 factor for the protein nanoparticles was calculated in the retentate as explained in [29].

154 **2.5 Protein quantification using size exclusion chromatography**

155 Feed, filtrate and retenate samples from filtration experiments were analysed with size exclusion

156 chromatography using Agilent 1260 HPLC system with a diode array detector. For TG and BSA, 50

157 µL of sample was injected onto a TSKgel3000SWXL (7.8 x 300 mm) with 30nm pores at a flow rate of

158 0.6 mL/min. For BSA NP, 20 µL of sample was injected onto a BioSEC5 (7.8 x 300 mm) with 100nm

159 pores at a flow rate of 0.8 mL/min. PBS was used as the equilibration and elution buffer for both

160 columns. Proteins were detected by measuring absorbance at a wavelength of 280 nm. Calibration of

161 the columns was tested using gel filtration standard from Biorad, UK.

162 **3. Results and discussion**

163 **3.1 Selection of the model protein solutes**

164 Bovine serum albumin (BSA) of 67kDa, thyroglobulin (TG) of 670kDa and albumin nanoparticles (BSA

165 NP) were chosen as model solutes for host cell proteins, small viral vectors such as adeno-associated

166 viruses and larger viral vectors such as adenoviruses respectively. The mean hydrodynamic diameter

167 of these solutes was measured to be ~8.7 nm for BSA, ~21 nm for TG and 80-90 nm for NPs as

168 shown in **Fig. 1** corresponding to the reported sizes of the abovementioned viral vectors [30].
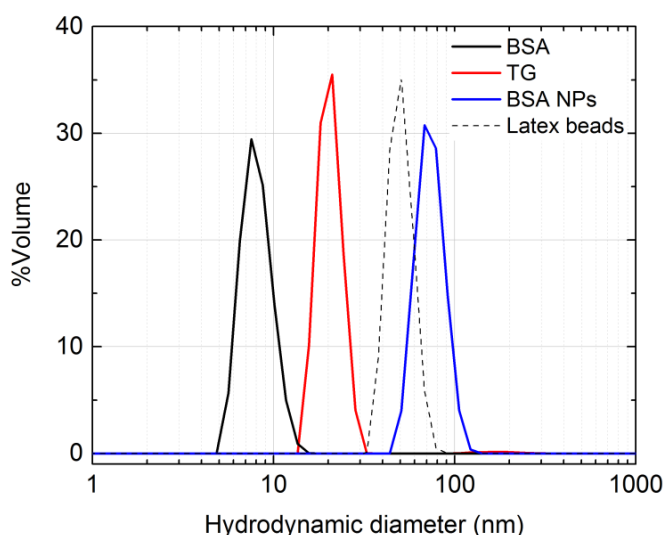
169

170 **Fig. 1 Particle size distribution of the three model solutes used in the present study obtained**

171 **from dynamic light scattering measured and analysed using Zetasizer NS (Malvern Panalytical,**

172 **UK) Monodisperse latex beads of 47 nm were used to check the calibration of the instrument.**

173 For nanoparticle preparation, more than 98% of the BSA was found to be converted into the
174 nanoparticles as observed using size exclusion chromatography. Both BSA and TG preparations also
175 had higher molecular weight components as shown by the size exclusion chromatography (see Fig.
176 A.1 for size exclusion chromatogram of BSA solution). The presence of these high molecular weight
177 components in BSA ranging from 66 kDa of the monomer and 300 kDa multimers is useful to
178 characterise the fractionation performance of the membranes if they are to be used to separate viral
179 particles from the smaller proteins impurities such as host cell proteins which have been reported to
180 be in range of 25 to 300 kDa with majority in range of 50-100 kDa [26].

181 **3.2 Selection of an appropriate polymeric ultrafiltration membrane for comparability studies**

182 Since polymeric ultrafiltration membranes are available in various ranges of materials and ratings,
183 selection of the appropriate membrane rating is crucial for proper comparison with the selected PAA
184 membranes. Commercial polyethersulfone (PES) membranes were selected over cellulose-based
185 membranes due to high permeability of the former as indicated by the manufacturer. Further,
186 polymeric membranes and porous anodic alumina membranes are rating differently. Membrane
187 ratings for polymeric membranes are usually expressed as their molecular weight cut off (MWCO)
188 limits in kiloDaltons using dextran sieving. PAA membranes on the other hands are rated by the mean
189 value of the pore size distribution of the active layer pores usually using electron microscopy.
190 Polymeric ultrafiltration membranes rated 100, 300 and 500 kDa were compared against the 20nm
191 rated PAA membrane for similar hydraulic permeability and dextran sieving characteristics.

192 Out of three rating for the PES membrane, 300 kDa PES was found to have the most similar hydraulic
193 permeability compared to the PAA membranes as shown in **Fig. 2 and Table 1**. Similar hydraulic
194 permeability would indicate similar convective mass transfer for solvent, and similar dextran sieving
195 characteristics would indicate similar intrinsic solute transport characteristics between the two
196 membranes. It should be noted that the coefficient of variation (CoV) of hydraulic permeability of the
197 membrane is higher for large MWCO polymeric membranes (10 and 37% for 500 and 300 kDa PES
198 membranes respectively) compared to the 20nm PAA (5% CoV) and 100kDa PES membrane (3%
199 CoV). Large coefficient of variation for the 300kDa PES membrane was attributed to filter to filter
200 variability as no outlier was detected in a dataset of 9 membrane discs from the same membrane lot.
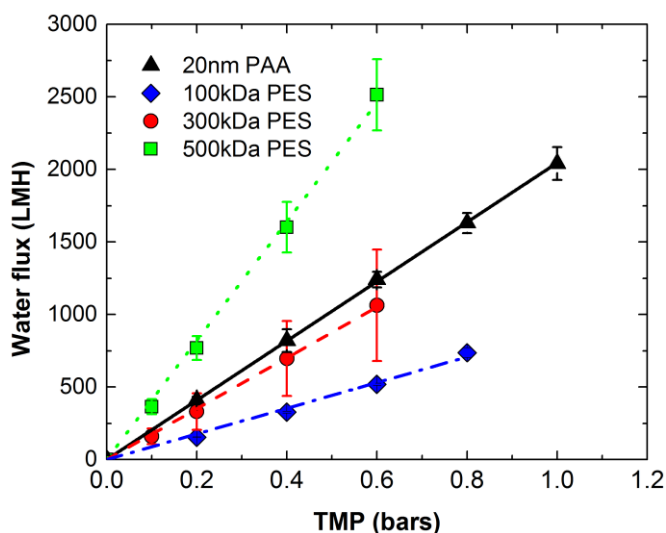
Fig. 2 Water fluxes at different transmembrane pressure for calculation of hydraulic permeability of 20nm rated PAA and PES membranes of different ratings. Fluxes were measured at room temperature (22-23°C) and using pre-filtered deionised water. The lines represent linear fit of the data points. The slope of the graph represents the hydraulic permeability value of the membranes and error bars represent one standard deviation across the mean values of flux for multiple membranes (n=9 for 300kDa PES and 20nm PAA; n=3 for 100 and 500 kDa PES). LMH represents the unit of flux in L m^{-2} hr^{-1}.

Dextran sieving curves, as shown in **Fig.3**, for both membranes were obtained using the same protocol. Though none of the polymeric membranes perfectly resembles the dextran sieving characteristics of the PAA membranes, sieving curve for the 300kDa polymeric membrane appears to be closer to that of the 20nm PAA membrane. Dextran ratings (for 90% rejection) obtained for both 300 and 500 kDa rated polymer membranes were larger compared to the ratings provided by the membrane manufacturer as shown in **Table 1**. Dextran rejection rating for 500kDa could not be measured as the value was beyond the exclusion limit (1000 kDa) for the size exclusion column used in the experiment. For the membrane rated 300kDa by the manufacturer, estimated dextran rating for 90% rejection was found to be 6 times larger than the specified rating. Such variations have been previously reported due to lack of a standardised dextran sieving tests resulting in variation of the methodology used including feed composition [31] and filtration modules [32] employed for dextran sieving tests. The stirred cell used in the current study was 25 mm in diameter which has been reported to have increased sieving compared to cells with larger diameters [32]. While larger stirred cells of 45 and 63 mm diameters were available, the largest available PAA membrane discs were 47 mm which were not compatible with either of the stirred cells. It was crucial to use the same stirred cell for both membranes to avoid different polarisation conditions due to the different size of modules.

7
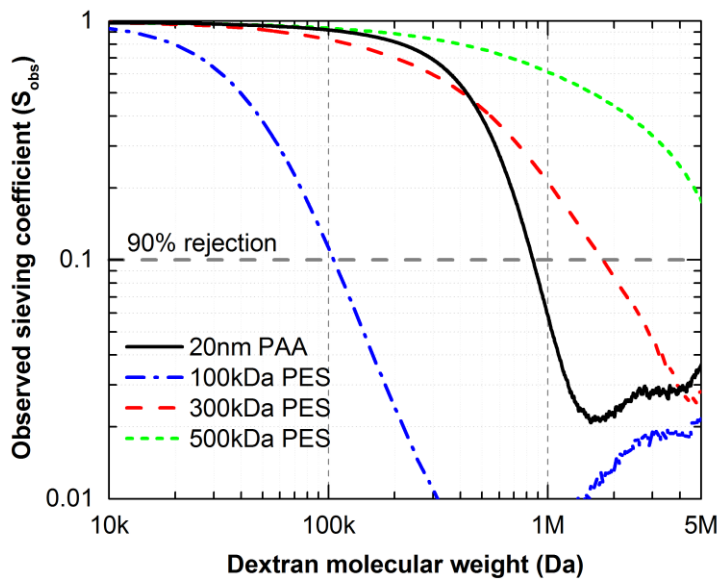
Fig. 3 Dextran sieving curves for porous anodic alumina (PAA) membrane rated 20nm and polyethersulfone (PES) membranes rated 100, 300 and 500 kDa. The horizontal grey line represents 90% rejection (observed sieving coefficient of 0.1) and is used to compare the dextran rating of the membranes by measuring corresponding values of X-axis at the point of intersection of the grey line and dextran sieving curve for each of the membranes.

A common dextran sieving test for PAA and PES membranes was useful to compare the effect of pore size distributions despite difficulty in the comparability of absolute ratings for the membranes. This is evident from the sharper curve obtained for the PAA membrane. Dextran being neutral solute does not have any electrostatic interactions with membrane material, and transport of dextrans is purely steric. Thus any variation in the solute transport should be purely due to membrane architecture and not affected by the surface chemistry of the membrane material. Hence for membranes with similar convection and dextran transport properties, any differences observed during protein filtration could be attributed to the mechanisms of retention and fouling. Differences in the membrane architecture were confirmed by imaging the active layer surface and cross-section of the PAA and 300kDa PES membranes. PAA membranes show straight pore channels and narrow pore size distribution of the active layer surface as shown in **Fig. 4**. Larger pores can be observed in the active layer surface of the 300 kDa PES membrane.

A

B

C

D
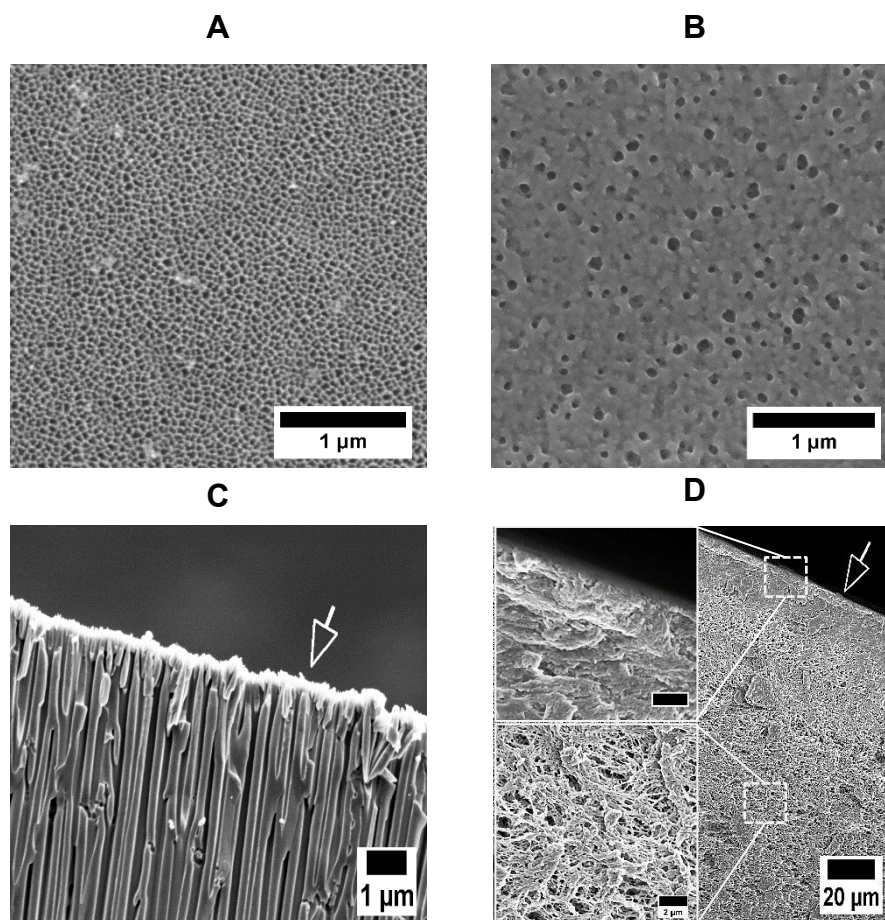
Fig. 4 Scanning electron microscopy images of the active layer surface (top) and cross section (bottom) of 20nm rated PAA (A and C) and 300 kDa PES membranes (B and D). Images of active layer surface (A and B) were obtained at the same magnification factor (50,000 X) for the membranes. Active and intermediate layers of the PES membranes are shown in the inset (scale bars = 2 µm) of D as 10-fold magnified images of respective areas. Arrows indicate the active layer side of the membranes. Images were obtained using InLens detector of Zeiss Gemini Sigma electron microscope (Carl Zeiss AG, Germany) at a gun voltage of 5kV after platinum coating of the samples.

| Membrane (With manufacturer specified ratings)	Hydraulic permeability (LMH/bar)	Dextran rejection (90%) rating (kDa)
100 kDa PES	890 ± 30	105
300 kDa PES	1750 ± 640	2000
500 kDa PES	4100 ± 420	NM
20 nm PAA	2050 ± 100	900

Table 1 Comparison of 20nm PAA membrane with various ratings of PES membranes by hydraulic permeability (mean value ± one standard deviation, n≥3) and dextran rejection rating. NM- not measurable

Based on hydraulic permeability and dextran sieving characteristics, we selected 300 kDa rated PES membranes for comparison with 20nm PAA membranes for further filtration experiments using the model protein solutes.

3.4 Filterability of solutions of the model protein solutes

PAA membranes showed better filterability for all protein solutions compared to the PES membranes as shown by higher cumulative filtrate fluxes in **Fig. 5**. As both membranes had different permeability the process flux values were normalised to the initial buffer fluxes measured at the same transmembrane pressure. PAA membranes operated at higher normalised flux values compared to the PES membranes even for BSA nanoparticles where the difference was smaller but still significant. Interestingly, the PES membranes operated at a value of 50% of the initial buffer flux for BSA filtration, but no flux decline was captured in the experimental data. This was likely due to the presence of the high molecular weight species (150-300 kDa) in the BSA preparations resulting in immediate clogging of some of the pores. It was found that the filter discs used for BSA filtration had very low permeability values (~900 LMH/bar) compared to the mean value for the entire lot (1750 LMH/bar). This was a result of random selection of the filter disc from same lot and high filter to filter variability with 300kDa PES membrane. Such low permeability value indicate a smaller mean pore size of the membrane which can make it susceptible to fouling by larger species in BSA feed. BSA did not result in any significant flux decline for PAA membranes as the membranes operated at ~90% value for the normalised flux throughout the filtration run which is discussed in next section when transmission of the solutes is compared.
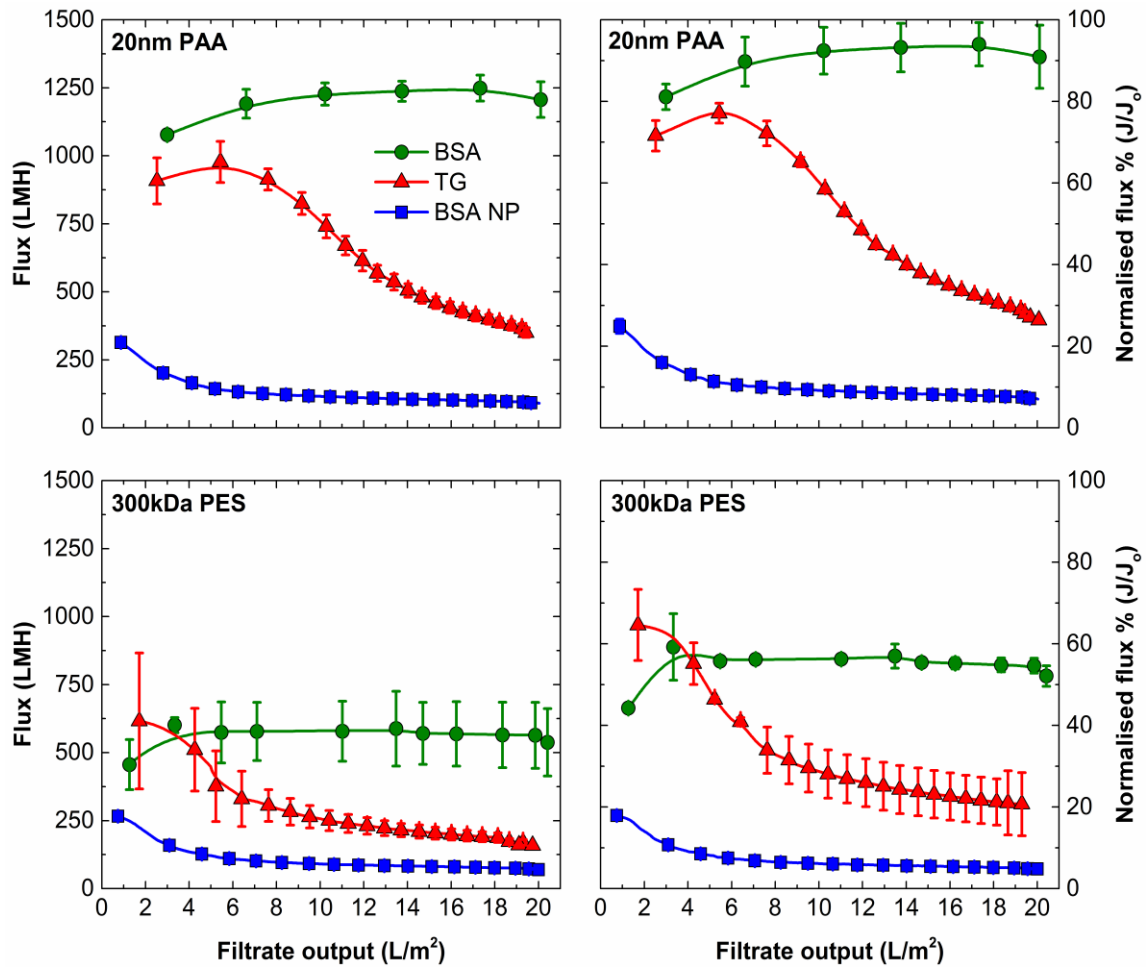
Fig. 5 Flux decline (absolute flux values on the left side plots and flux normalised to the initial buffer flux on the right side plots) observed for filtration of solutions of model protein solutes through 300 kDa rated PES and 20 nm rated PAA membranes. Symbols and error bars represent the average values and one standard deviation respectively for triplicate filtration runs. The transmembrane pressure of 0.6 bar and a stirring rate of 1500 rpm was used.

TG and BSA nanoparticles resulted in significant flux decline for both membranes as filtration progressed. However, the shape of the flux decline curves for TG was different for both membranes suggesting different mechanisms of the flux decline. Analysis of the raw filtration data (volume and time) for identification of the dominant fouling mechanism was carried out as described by Bolton et al., [27]. Models were constrained to a single output parameter by using the experimental values of initial buffer flux through the membrane. Mathematical expressions and the results of curve fitting are provided in table B.1 and B.2 respectively in appendix B.

Fig. 6 shows curve fits for the TG and BSA nanoparticle filtration with four fundamental mechanisms of the fouling. The best curve fit with the highest regression coefficient and lowest sum of the square of residuals (SSR) was interpreted as the dominant fouling mechanism responsible for the flux decline. As speculated from the flux decline curves, mechanisms of fouling by TG were different for the two membranes. Intermediate blocking was identified as the dominant mechanism of flux decline

293   in the PAA membrane, and cake filtration was dominant for the PES membrane. For BSA

294   nanoparticles, the quality of the curve fitting was not as good as obtained for TG. Both membranes

295   showed cake filtration as the closest best fit with the experimental filtration data. Interestingly, both

296   membranes showed high flux decline in the initial filtration period where experimental data is well

297   below the best-fit curve for cake filtration. It suggests that the mechanism of flux decline for BSA

298   nanoparticles has 'cake-like' resistance for convection across the membranes. It should be noted that

299   the confidence on the validity of these model fits for BSA nanoparticles is low as the value of sum of

300   the squares of residuals (SSR) was about a magnitude higher compared to those observed for TG

301   filtrations. SEM images of the BSA NP fouled surfaces of the membranes (Fig. C.1 and Fig D.1 in

302   Appendices) also do not show a thick and uniform layer. It is more likely that flux decline is through a

303   different mechanism such as osmotic pressure or concentration polarisation. It is also possible that

304   multiple fouling mechanisms are responsible for such behaviour. Combined models of fouling were

305   attempted but the fits were over-parameterised, thus not considered valid. It should be noted that

306   models of the fouling mechanisms are often developed and validated for microfiltration or depth

307   filtration membranes and for purely dead-end filtration without any stirring on the membrane surface.

308   Our experiments were performed using the dead-end mode with high stirring speed above the

309   membrane surface which will impact cake as well as concentration polarisation above the membrane

310   surface.
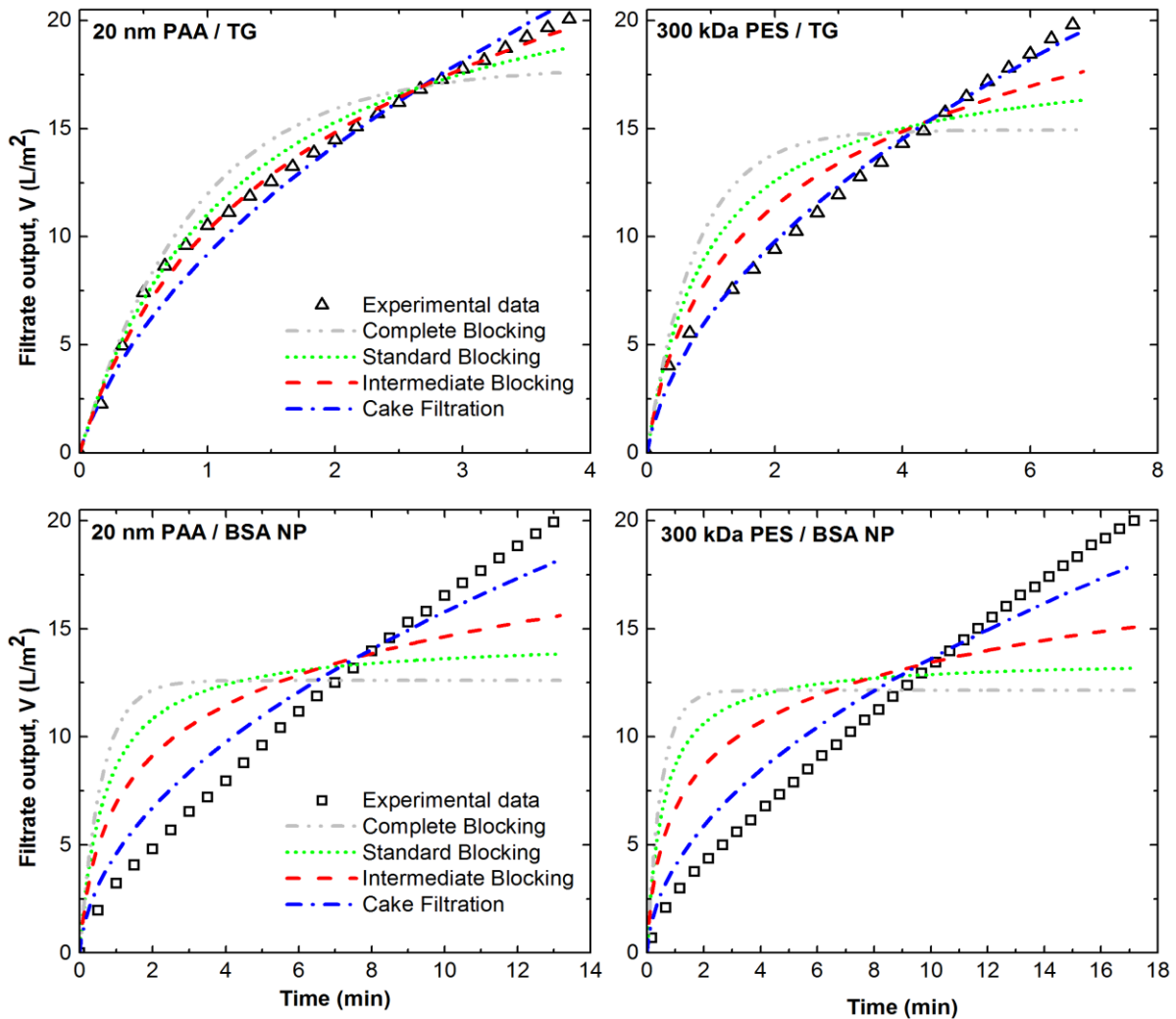
Fig. 6 Experimental data (open symbols) for TG and BSA nanoparticle filtration through PAA and PES membranes along with best-fitted curves (lines) for four fundamental mechanisms of fouling. Filtrate output is normalised with the membrane area. Mathematical expressions of the fouling models used and output data for curve fitting including goodness-of the fit data is given in table B.1 and B.2 respectively in appendix B.

3.5 Transmission of the model protein solutes

Both membranes show high transmission of BSA (>95%) and transmission of the solutes reduced with an increase in the solute size as expected. PAA membranes, however, showed a higher transmission of the larger model solutes (TG and BSA NP) compared to the PES membrane as shown in **Fig. 7.** Higher transmission of BSA nanoparticles through 20nm PAA membranes was unexpected as nanoparticles are more than 2-3 folds larger than the pore rating of the PAA membranes. SEM analysis of the active layer surface of the PAA membranes revealed that the mean pore size of the active layer surface was larger than 20nm pore rating. A mean pore size of 55±7 nm was estimated from image analysis of the SEM images of active layer of the membranes using Image J, but the distribution was narrow and maximum pore diameter was not larger than the mean size of nanoparticles. Pore size distribution of the 300 kDa PES membrane showed the presence of large

13

328 pores and despite this lower transmission of BSA NP was observed. Pore size distributions of
329 membranes are provided in Appendix F. Particle size distribution of the retentate obtained using PAA
330 membrane did not show any significant difference from that of the initial feed solution which ruled out
331 a favourable transmission of a sub-population of BSA NP (with size smaller than 55 nm) through
332 larger pores in the pore size distribution of the PAA membrane. SEM imaging over a broad surface
333 area of the PAA membranes revealed patches of the surface where the active layer was missing as
334 shown in **Fig. 8**, exposing the support layer underneath which has a larger mean pore diameter of
335 ~200 nm. Such large defects have been reported in commercial PAA membranes [18] and are
336 attributed to the fabrication conditions.
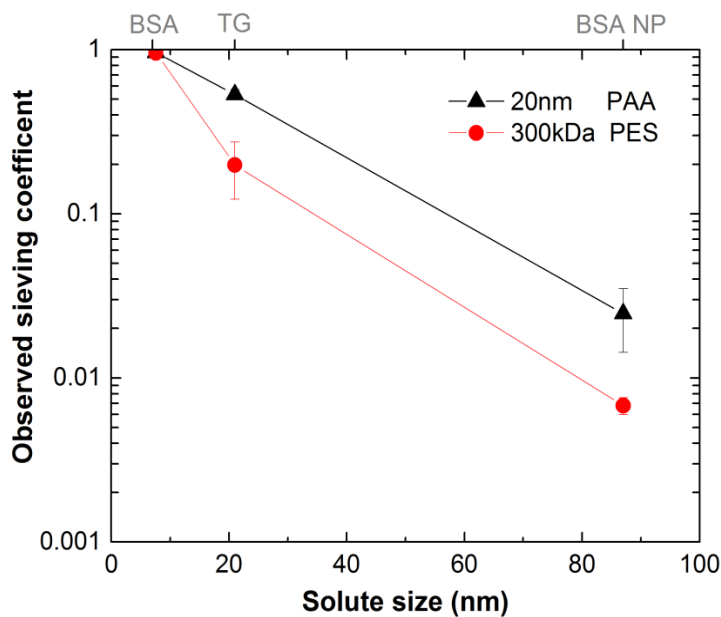
337

338 **Fig. 7 Transmission of different model solutes through 20nm rated PAA, and 300 kDa rated**
339 **PES membranes. Observed sieving coefficient represents the ratio of the solute concentration**
340 **in the collected filtrate and initial feed solution. Data points and error bars represent average**
341 **values for triplicate runs and one standard deviation across the average respectively.**

342 The presence of these large surface defects could explain almost four-fold higher transmission of the
343 BSA nanoparticles through the PAA membrane. Random distribution of these large defects and
344 limited scanning area capability of SEM makes it difficult to obtain an accurate count of such defects
345 and their contributions to the buffer flow rate and solute transmission across the membrane. Since
346 defect free membrane discs were not available, the impact of these surface defects on the hydraulic
347 permeability of the membrane could not be experimentally measured. Even higher hydraulic
348 permeability of 1.2047×10^{-8} m/Pa.s (~2 times than 5.7×10^{-9} measured in this study) has been
349 previously reported [19] for 20nm PAA membrane indicating that such density of such large surface
350 defects may even vary among different membrane lots. Compromised sealing of the PAA membrane
351 discs due to the support ring on the membrane disc was ruled out since reasonable water flow rates
352 were observed through the membranes even at high pressure (1 bar). Also a compromised sealing
353 would likely result almost complete solute transmission even for large solutes which was not

observed. Higher transmission of protein solutes through the PAA membrane was also the opposite of

the trend observed for sieving of the large dextrans as shown in **Fig**. **3**. Especially for a molecular

weight of 670kDa, which is the molecular weight of thyroglobulin, sieving coefficients for thyroglobulin

and dextran molecule of same molecular weight were found to be 0.60±0.04 and 0.21±0.01

respectively. Likely reason for lower sieving coefficient for dextran molecules could be due to larger

hydrodynamic size of the dextran. Stokes diameter for 670kDa dextran molecule was calculated to

~36 nm, larger than ~16 nm calculated for 670 kDa thyroglobulin molecule using M.W. and Stokes

radius correlation described elsewhere [33]. For 300kDa PES, observed sieving coefficients were

higher for thyroglobulin (0.21±0.08) compared to dextran of equal molecular weight (0.39±0.08). Lutz

[33] have pointed out that due to linear shape of the dextrans, the molecules will tend to align with

their larger diameter perpendicular to the pore entrance thus resulting in larger transmission

compared to the globular molecules like proteins. This hypothesis appears to be true for PES

membranes. Besides size differences other possible explanations for this could be the very low

polarising operating conditions of the dextran sieving experiments (constant flux of 5 LMH and stirring

speed of 1000 rpm compared to variable flux of 2400 to 70 LMH for protein filtration experiments

under constant positive pressure of 0.6 bar), the neutral charge of the dextrans and linear shape of

the dextran molecules in contrast to the charged and globular protein solutes. It is unclear if the

membrane architecture and surface defect of PAA membranes played a role in differences in the

sieving of dextran and protein molecules.
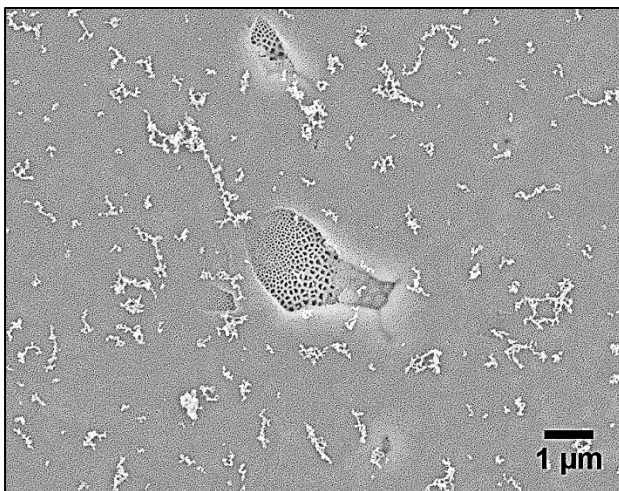
Fig. 8 A low-resolution image of the active layer surface of the 20nm rated PAA membranes obtained using a scanning electron microscope (Gemini sigma, Carl Zeiss AG, Germany) showing the large surface defects exposing the underlying support layer with pores of ~200nm diameter.

3.6 Restoration of membrane permeability post filtration

Fig. 9 shows the distinct performance of the two membranes when compared by membrane

permeability post-filtration of different solutes. Restoration of the membrane permeability is indicated

by a high value of the flux recovery ratio (FRR). Loosely deposited protein on the membrane surface

382   was removed by thoroughly rinsing the membrane surface using buffer solution before measurement

383   of the post-filtration buffer flux. Rinsing the stirred cell also ensured that post filtration buffer flux

384   would not be affected by the residual solute bound on the stirred cell surface. Thus, low FRR values

385   indicate tightly bound proteins on either membrane surface or inside membrane bed which would

386   require physical or chemical treatment for removal. The membrane surface when examined using

387   electron microscopy showed patches of the fouling (see Fig. C.1 and D.1) though the coverage of the

388   membrane surface cannot be correlated with the value of FRR thus suggesting a role of the internal

389   fouling. For both membranes, FRR values were found to be minimum for the filtration of TG. SEM

390   images of the active layer surface of the membranes also showed similar trend with maximum fouling

391   observed for TG fouled membranes (see fig. C.1 and D.1).

392
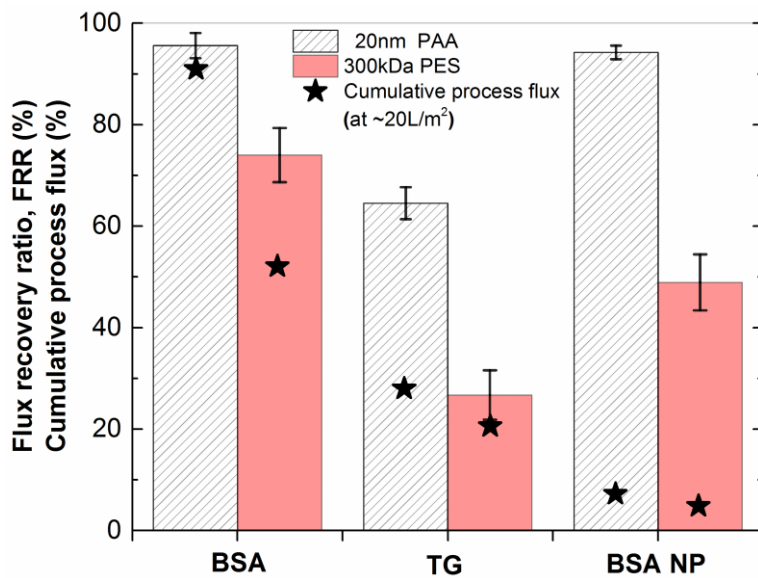
Fig. 9 Recovery of membrane permeability after filtration of different model solutes (BSA, TG
and BSA NP) measured as flux recovery ratio (post-filtration buffer flux as % of the initial
buffer flux). Columns represent average value of FRR for triplicate filtration runs and error
bars represent one standard deviation across the average value. Star symbols on columns
represent the values of the cumulative process flux observed at the end of the filtration (as %
of the initial buffer flux) for corresponding membranes and solutes.

399   The PAA membrane showed highest internal fouling by TG as indicated by lowest FRR value of 60%

400   among all three solutes. Hydrodynamic diameter of TG is measured to be ~22 nm which is

401   approximately half of the measured mean pore size of 55 nm for the PAA membranes used. Though

402   high transmission of TG could be explained due to the presence of surface defects, it appears that

403   pores in the distribution may also have been accessed by the TG particles eventually blocking them.

404   This is also apparent from the intermediate blocking fouling model predicted for TG filtration where a

405   few particles initially plug some pores and rest of the particles deposit on the plugged pores. SEM

406   images of the TG fouled membrane also show fouling embedded on smaller pores of the membranes

407   (Fig. C.1). Interestingly, both BSA and BSA NP, showed very high FRR values above 90%. For BSA,

408   which has an average hydrodynamic diameter of 8.7 nm, approximately 6 fold lower than the pore

409   size, pore plugging would only be for the pores at the lower end of the pore size distribution. It should

410   also be noted that average hydrodynamic diameter of BSA also has contribution from the minor HMW

411   component of the BSA solution and actual hydrodynamic diameter of smaller BSA monomers may be

412   smaller than 8.7 nm, thus having high sieving of the BSA from the pores. With a mean diameter of 80

413   nm the BSA NPs are unlikely to enter the smaller pores in the intact active layer of the PAA

414   membrane. FRR value of more than 90% was observed for 80nm BSA NP indicating very little pore

415   plugging by FRR. Restoration of membrane permeability with a simple wash of the membrane surface

416   after protein filtration suggests that the flux decline for BSA nanoparticle filtration is through a

417   pressure dependent and reversible mechanism which manifests immediately as pressure is applied.

418   Concentration polarisation is a pressure dependent and reversible phenomenon which manifests due

419   to an imbalance in solute mass-transfer from bulk solution towards the membrane surface and away

420   from it. Reversibility of the membrane permeability has been previously associated with concentration

421   polarisation based flux decline [34]. SEM image of the active layer surface also shows only a few

422   pores blocked by BSA NP (Fig. C.1).

423   For the PES membrane, FRR values were significantly lower than those of PAA membranes for all

424   solutes. Notably, only 70% of the initial membrane permeability is restored after filtration of BSA

425   where membranes operated at 50% of the initial buffer flux during the filtration as shown in fig 5. This

426   was likely due to internal fouling caused by high molecular weight components (>150 kDa) observed

427   in the BSA solution. Among all the solutes, the lowest FRR value (~20%) was obtained for TG,

428   indicating higher internal fouling. The likely reason is that the molecular weight of TG (660 kDa) is

429   close to the molecular weight cut off of 300 kDa for the membrane, thus making the larger pores of

430   the membrane accessible to the solute. Cake like protein depositions were also observed on the

431   membrane surface fouled by TG when observed using electron microscopy (Fig. D.1). Curve fitting

432   with fouling models also identified cake filtration as the dominant mechanism of fouling for TG filtration

433   through PES membranes. Filtration of BSA nanoparticles showed an FRR value of 50% significantly

434   lower than 95% observed for PAA membranes and significantly higher level of fouling observed on

435   active layer surface of the PES membrane as observed using SEM. Higher fouling of the PES

436   membrane by BSA NP could not be explained with the cake filtration model only. Further, coverage of

437   the membrane surface area by BSA NP fouling was not very high indicating presence of internal

438   fouling. Membrane compressibility is unlikely as the polymeric membranes were operated at a

439   transmembrane pressure lower than the maximum operating pressure specified.

440   The role of solute-membrane interactions to fouling such as electrostatic binding can be ruled out as

441   both membranes have been marketed as low protein binding materials and experiments were carried

442   out at a moderate salt concentration to minimise such non-specific binding. We suggest that the

443   concentration polarisation is the dominant flux decline mechanism for both membranes in the initial

444   filtration window especially for BSA NP. Since the concentration polarisation has been known to

445   increase the leaky transmission of the polarising solute through the membranes [35, 36], model

446   solutes will likely diffuse into the larger pores in the pore size distribution of the membranes. Pores

447   larger than the nanoparticles were observed on the active layer of the PES membranes and in the

surface defects on the active layer of PAA membranes exposing the large pores of the support layer of the membrane underneath. We hypothesise that the differences in the membrane architecture of the two membranes result in different particle retention mechanisms. PAA membranes are thinner (~60 μm) and have near straight channels (low tortuosity). In contrast, the polymeric membrane has thicker active and intermediate layer (~120 μm) with highly tortuous channels. Effective diffusional paths for solute particles would be higher for the polymeric membranes compared to the thinner and straight channels of the PAA membranes. Thus, protein nanoparticle diffusing through the smaller and straight channels of the support layers exposed by defects in the PAA membrane will face less resistance compared to diffusion through large surface pores into the tortuous channels across a thicker membrane bed of the PES membrane. This would result in higher transmission of particles through surface defects of PAA membranes without clogging of the smaller pore on the intact active layer of the membrane. Nanoparticles would gradually deposit inside the PES membrane channels due to the highly tortuous path and collision to the channel walls resulting in internal fouling and low transmission. The proposed hypothesis is illustrated in **Fig. 10**.
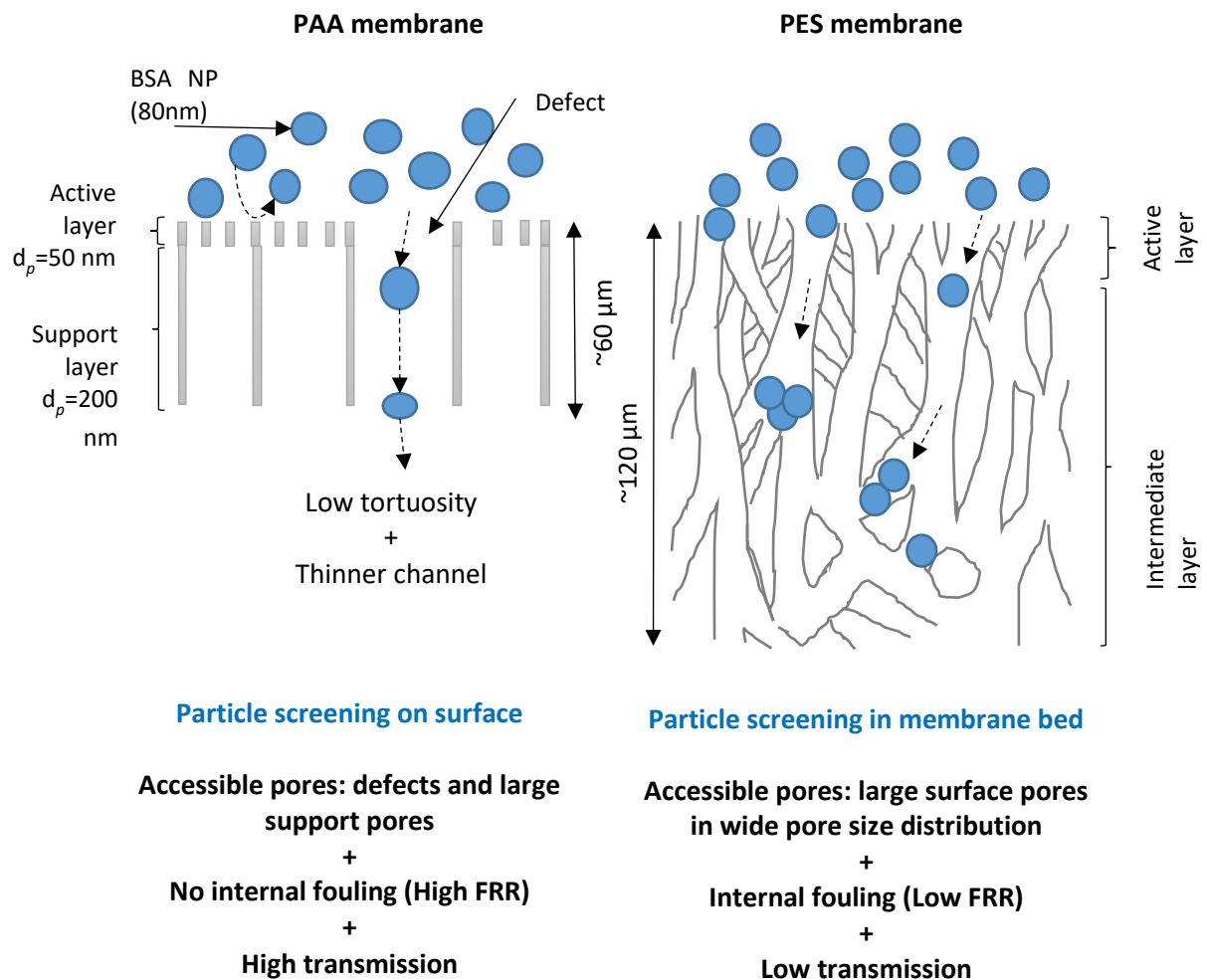
Fig. 10 Proposed hypothesis for the role of membrane architecture in different particle screening behaviour of the PAA and PES membranes resulting in different fouling and transmission characteristics

18

3.7 Comparison of single solute and binary mixture filtrations

Application of the PAA membranes in the fractionation of virus particles and cell culture impurities will require characterisation of the separation performance of the membranes. For this purpose, a binary mixture of TG and BSA NP, the model solutes for viral particles with BSA were filtered through membranes with BSA used as the model impurity. The comparison showed no differences in the average flux and value of FRR % when compared to the single solute filtrations of fouling solutes (TG and BSA NP) suggesting no further interaction of BSA and the large solutes in the internal fouling of the membrane.

Feed	Solutes	Observed sieving coefficients, S_{obs}	
		20 nm PAA	**300 kDa PES**
Single solute	BSA	**0.96 ± 0.03**	**0.96 ± 0.02**
	TG	0.60 ± 0.04	0.21 ± 0.08
	BSA NP	0.03 ± 0.01	0.01 ± 0.00
Binary solutes BSA + TG	BSA	**0.89 ± 0.03**	**0.76 ± 0.01**
	TG	0.67 ± 0.09	0.43 ± 0.03
Binary solutes BSA + BSA NP	BSA	**0.68 ± 0.03**	**0.54 ± 0.06**
	BSA NP	0.18 ± 0.03	0.00 ± 0.00

Table 2 Transmission of model solutes in single solute filtrations compared to transmissions observed in filtrations of binary solute mixtures (BSA with TG or BSA NP). Data represents average values ± one standard deviation for triplicate filtration runs.

Transmission of the respective solutes during filtration of single solute and binary solutes feed are compared as shown in **Table 2**. For the PAA membrane, the transmission of TG did not change significantly for the filtration of the binary solute mixture and single solute solution. BSA NP showed unusually high transmission through the PAA membrane in the binary solute feed. For PES membranes, TG transmission was almost two times higher for the binary solute feed compared to the single solute feed. This could be due to the high variability in the hydraulic permeability of the membrane discs of PES membrane even when same membrane lot was used. The membrane discs used for BSA+TG filtration had a hydraulic permeability of 1930 ± 120 LMH/bar compared to 1600 ± 540 LMH/bar used for the filtration of TG alone. Transmission of BSA NP in the PES membranes however remained unaffected by presence of BSA in the feed. Transmission of BSA was however affected by the fouling by larger solutes as a lower sieving coefficient of BSA was observed during filtration of binary solute mixtures as shown in table 2. Unusually high transmission of BSA NP in binary feed filtration through PAA membranes could not be explained as the same lot of the membrane was used for single, and binary mixture filtrations along with same nanoparticle batch were used. Nonetheless, it was clear from this experiment that transmission of smaller solutes such as BSA is significantly reduced in the presence of large fouling solutes resulting in lower selectivity that

493   indicated by filtrations of the single solute feeds. As both membranes showed high retention of the

494   protein nanoparticles, membranes could be used for fractionation of the binary mixtures of large

495   protein nanoparticles and a smaller impurity such as BSA. Fractionation was however incomplete in

496   this experiment where mixtures were filtered through membranes or feed was concentrated.

497   To increase the fractionation, a filtration strategy involving multiple passes of feed or diafiltration could

498   be used. This diafiltration based fractionation process was carried out to study separation

499   performance and filterability of the mixtures of BSA nanoparticles and BSA through PAA and PES

500   membranes including the effect on the internal fouling of the membrane upon a lengthy process as

501   would be encountered in actual processing conditions.

502   **3.8 Fractionation of mixtures of model protein solutes (BSA NP and BSA) using discontinuous**

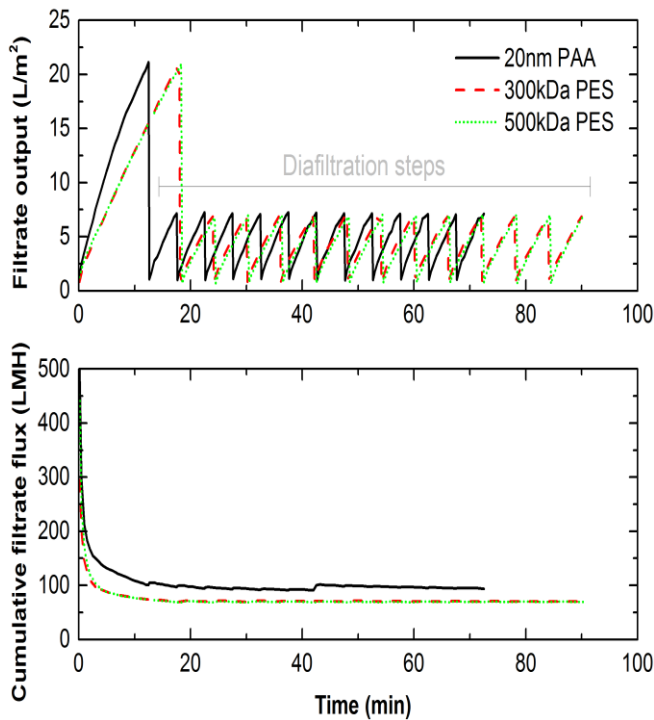503   **diafiltration**

504   Discontinuous diafiltration was used to improve the fractionation of mixtures of BSA nanoparticles and

505   BSA. Discontinuous or sequential diafiltration was used after an initial concentration step

506   concentrating the protein mixture to 4-fold volumetrically. A total of 12 diafiltration steps (including 2-

507   fold dilution of retentate followed by 2-fold concentration) were carried out resulting in a total of 12

508   diavolumes of the buffer exchanged. Final retentate solution was analysed using size exclusion

509   chromatography.

510    $$\text{Purification factor, PF} = \frac{\text{Yield}_{\text{(BSA NP)}}}{\text{Yield}_{\text{(BSA monomer)}}}$$

511   **Fig. 11** shows the fractionation experiment in discontinuous diafiltration mode and the flux decline

512   observed. PAA membranes showed significantly higher filtrate flux throughout the filtration run with

513   cumulative filtrate flux value of ~97 LMH compared to ~70 LMH for both PES membranes. This

514   resulted in shorter process time of ~70 minutes for 12 diavolumes diafiltration in PAA membranes

515   compared to ~90 minutes for the polymeric membranes. Note that both PES membrane ratings

516   showed similar flux despite different hydraulic permeability suggesting higher fouling in the 500kDa

517   membrane as hydraulic permeability of the 500 kDa membrane is approximately two times higher

518   than that of 300kDa PES or 20 nm PAA membrane.

519   PAA membranes showed three times higher purification factor compared to both polymeric

520   membranes. This is due to high BSA NP retention, and low residual BSA detected in the retentates as

521   shown in chromatograms of **Fig. 12** and tabulated in **Table 3**. The 300kDa PES membrane retained

522   almost all of the nanoparticles, but also had high residual BSA in the retentate. There appears to be a

523   trade-off between the purification factor and BSA NP yield for the membranes studied. In the real-

524   world biologics purification processes, purification factor of 780 as observed for the 300kDa PES

525   membrane may be sufficient given that it also results in highest recovery of BSA NP. However, the

526   choice of a membrane for fractionation may also be governed by other factors such as absolute

527   impurity levels, net impurity exposure to patient depending upon the dosage and process optimisation

528   factors (diavolumes required and membrane fouling). Limited fouling was observed for PAA

529 membranes as FRR of 96% was measured after protein filtration. Fouling was more significant in the

530 PES membranes as only 33, and 14% of the initial buffer flux could be recovered for 300 and 500 kDa

531 ratings respectively. The diafiltration step also appears to result in increased fouling in the PES

532 membrane as compared to the initial concentration step. This is evident from the reduction in the FRR

533 % from ~50% (as shown in **Fig. 9**) to 33 % for BSA NP and BSA mixture. Both PES membranes

534 required additional chemical treatment for removal of the internal fouling and restoration of membrane

535 permeability details of which are available in the **Fig. E.1** in the appendix section**.**

536

537 **Fig. 11 Fractionation of mixture of BSA and BSA NP using 20nm rated PAA, 300 and 500 kDa**

538 **PES membranes. The top chart shows the initial concentration step (filtrate output to 20 L/m²**

539 **during initial 20 minutes) and discontinuous diafiltration mode used for fractionations, and the**

540 **bottom chart shows cumulative filtrate flux during the initial concentration and subsequent**

541 **diafiltration phase. Initial membrane loadings for all the membranes were equal and similar**

542 **diafiltration strategy (diavolumes per step and total diavolumes) was used.**

Membrane	% BSA removal (permeate)	% BSA NP retention	% residual BSA (retentate)	Purification Factor (BSA NP)	FRR (%)
20nm PAA	95 ± 3	86 ± 6	0.04 ± 0.00	2170 ± 200	96
300kDa PES	92 ± 3	100 ± 7	0.13 ± 0.01	780 ± 80	33
500kDa PES	93 ± 3	82 ± 6	0.10 ± 0.00	990 ± 100	14

Table 3 Performance of different membranes for complete fractionation of mixtures of BSA NP and BSA. Data represents average values ± one standard deviation for triplicate measurements.
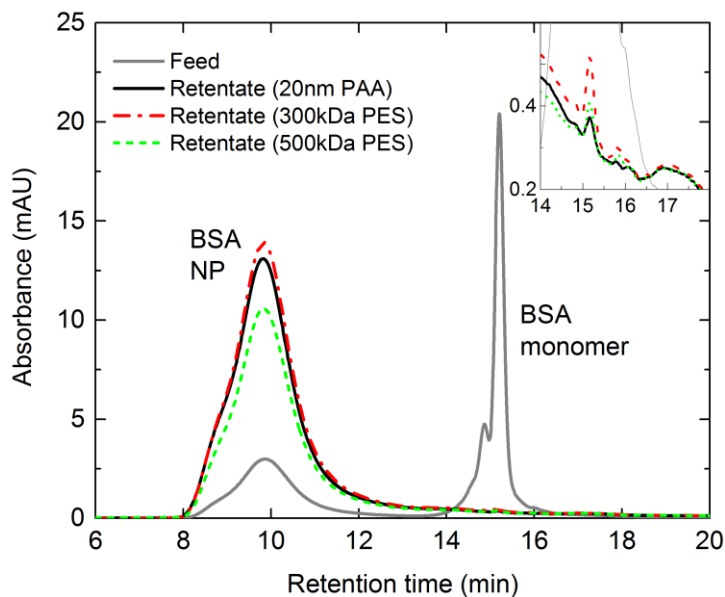
Fig. 12 High performance–size exclusion chromatograms for initial feed (BSA NP + BSA) and retentate obtained after 12 diavolumes of diafiltration performed using different membranes (20nm PAA, 300 and 500kDa rated PES membranes). Figure in the inset shows the peak of residual BSA monomer in the retentate solutions. Volume concentration factor for retentate is ~4 in relation to the feed volume. Chromatograms were obtained using BioSEC-5 column (7.8 x 300 mm) at a flow rate of 0.8 ml/min with PBS as elution buffer and diode array detector for measurement of absorbance by proteins at a wavelength of 280 nm.

4. Conclusions

To the best of our knowledge, this was the first study comparing conventional polymeric membranes with the porous anodic alumina under the same filtration conditions. Previous studies by Prádanos et al. [19, 20] and Lee et. al. [18] have studied PAA membranes with proteins but did not offer any comparison with traditionally used polymeric membranes. A significant challenge in such a comparison was the different rating standards used for PAA and polymeric ultrafiltration membranes. Therefore membranes were first experimentally matched on the basis of hydraulic permeability and dextran sieving characteristics. This was performed for a 20nm rated PAA membrane and compared to three ratings of PES membranes. It was found a 300 kDa rated PES membrane matched most closely. Interestingly, the dextran sieving curve for the PAA membrane was sharper than that of the PES membranes highlighting the narrow pore size distribution of these membranes.

Using the matched PAA, PES membranes an experimental design was chosen to characterise the filtration and separation performance of the two membrane types for viral vector purification. This characterisation was done using large solutes like thyroglobulin (~22 nm hydrodynamic diameter) and

BSA nanoparticles (~80 nm diameter) as mimics of common viral vectors such as AAVs and AdVs respectively. PAA membranes exhibited 3-4 fold higher transmissions of these mimics as well as 2-3 fold higher fouling resistance in comparison to the PES membrane. Both membranes are unsuitable for ultrafiltration of smaller viruses such as AAVs as the mimic solute thyroglobulin was only partially retained and significantly fouled both of the membranes. For BSA nanoparticles (the AdV mimic), both membranes are highly retentive, and PAA membranes show remarkably high restoration of permeability above 90% of the initial value compared to 50% for PES membranes upon rinsing the membrane and stirred cell surfaces with the buffer solution. PAA membranes also exhibited robust separation performance for a complete fractionation of a binary mixture of BSA and BSA nanoparticles in an extended diafiltration process. PAA membranes showed 30% higher flux and 3-fold higher purification factor for BSA nanoparticles in comparison to the PES membrane and more than 90% of permeability restored while the PES membrane fouled much more extensively with only 33% of the permeability restored which necessitated a chemical cleaning.

We propose that the observed differences in the filtration and separation performance of the two membranes are a result of significant differences in their architecture giving rise to different screening mechanisms. PAA membranes screen large solutes like BSA nanoparticles above membrane surface due to a smaller and narrow pore size distribution resulting in very low fouling. PES membranes on the other hand allow such solutes to enter the membrane through the larger pores of the wider pore size distribution typical of this membrane type, but eventually trap these particles within the tortuous pore channels of the thicker PES membrane resulting in higher internal fouling. Leaky transmission of solutes seen in the PAA membranes is likely due to some defects on the active layer allowing access to the highly permeable straight pore channels of the support layer. Low fouling and high nanoparticle retention make PAA membranes an attractive candidate for ultrafiltration of sensitive biomolecules such as viral vectors by reducing process time by reducing the requirement of chemical cleaning in between batches.

To further the development of PAA membranes for virus ultrafiltration, fabrication of defect-free membranes should be studied to reduce their susceptibility to loss of performance due to these defects. To substantiate the proposed screening mechanisms of the two membrane types, direct observation of the location of the fouling in the membrane bed could be performed using fluorescently tagged solutes and confocal laser scanning microscopy. Another extension of the present work would be to use a real viral feed and cross flow conditions to leverage high mass transfer characteristics of this mode of operation with representative feed materials. The brittle and fragile nature of PAA membranes may pose a challenge to their adoption at industrial scale so alternative membrane materials with similar membrane architecture should be considered. One such alternative is self-assembled block copolymer membranes.

Acknowledgements

Appendices

Appendix A. Size exclusion chromatogram of BSA solution used in filtration experiment showing high molecular weight (HMW) components
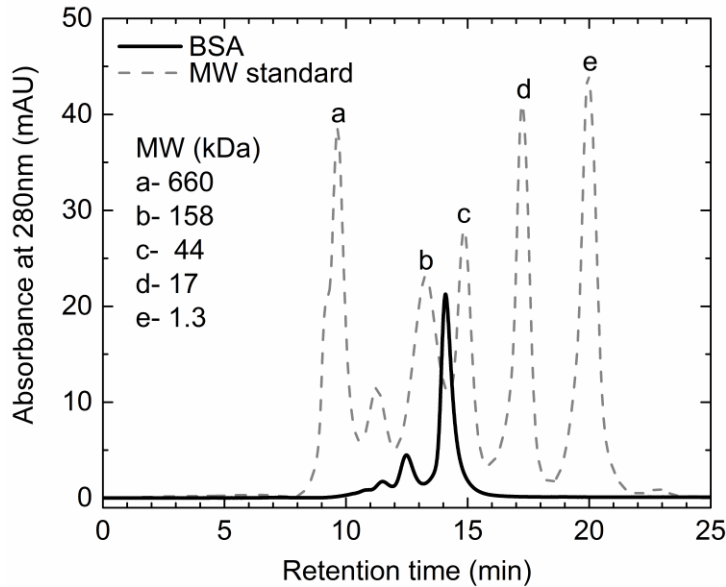
Fig. A.1 Chromatogram overlay of the molecular weight (MW) standard (dashed line) and the BSA solution (solid line) obtained using a size exclusion column, TSKgel3000SWXL at a flow rate of 0.6 mL/min under isocratic elution with PBS (detailed method is described in section 2.5). Peak labels represent the molecular weights (kDa) of the peak proteins in the standard.

BSA monomer (~67 kDa) corresponds to the major peak at the retention time of 14 minutes in the chromatograms. Chromatogram also shows the presence of the high molecular weight components (peaks with retention time below 14 min) in the BSA solution. Relative amount of these high molecular weight components in BSA solution was estimated to be ~23% from the peak area%.

Appendix B. Mathematical expression for various mechanisms of fouling and results of the

619 **curve-fitting of the experimental data with mathematical expressions of mechanisms of fouling**

Mechanism	Mathematical expression for filtrate volume, V (m^3/m^2)
Standard blocking	$V = \left(\dfrac{1}{J_o t} + \dfrac{k_s}{2} \right)^{-1}$
Complete blocking	$V = \dfrac{J_o}{k_b} \left(1 - \exp(-k_b t) \right)$
Intermediate blocking	$V = \dfrac{1}{k_i} \ln(1 + k_i J_o t)$
Cake filtration	$V = \dfrac{1}{k_c J_o} \left(\sqrt{(1 + 2 k_c J_o^2 t)} - 1 \right)$

620

621 **Table B.1 Mathematical expressions of the fundamental mechanisms of fouling in constant**

622 **pressure filtrations as described by Bolton et al. [27] and used in this study.**

623 A mechanism is identified to be dominant mechanism by fitting these expressions to the experimental

624 filtration data (volume filtered per unit membrane area, V (m^3/m^2); time, t (sec) and initial buffer flux, J_o,

625 (m/s)). k_x represents fouling constants for respective models with different units for different

626 mechanisms.

627 **<u>Results of curve fitting of the filtration data with mathematical models of fouling</u>**

Fouling mechanism		BSA nanoparticles			Thyroglobulin		
		SSR (x 10^{-3})	R^2	Parameter	SSR (x 10^{-4})	R^2	Parameter
20nm PAA	Standard	1.24 ± 0.06	0.49	k_s = 137 ± 1	0.07 ± 0.04	0.99	k_s = 78 ± 2
	Complete	1.78 ± 0.78	0.27	k_b = 0.03	0.30 ± 0.11	0.95	k_b = 0.02
	Intermediate	0.65 ± 0.02	0.73	k_i = 278 ± 5	**0.02 ± 0.00**	**1.00**	k_i = 112 ± 4
	Cake	**0.13 ± 0.00**	**0.94**	k_c (x 10^{-6}) = 4.4 ± 0.2	0.15 ± 0.03	0.98	k_c (x 10^{-6}) = 0.64 ± 0.1
		SSR (x 10^{-3})	R^2	Parameter	SSR (x 10^{-3})	R^2	Parameter
300kDa PES	Standard	1.83 ± 0.14	0.40	k_s = 145 ± 1	0.17 ± 0.05	0.85	k_s = 100 ± 7
	Complete	2.45 ± 0.16	0.20	k_b = 0.03	0.33 ± 0.07	0.71	k_b = 0.02
	Intermediate	0.95 ± 0.08	0.70	k_i = 321 ± 4	0.08 ± 0.03	0.94	k_i = 160 ± 20
	Cake	**0.17 ± 0.02**	**0.94**	k_c (x 10^{-6}) = 5.8 ± 0.3	**0.01 ± 0.01**	**0.99**	k_c (x 10^{-6}) = 1.7 ± 0.3

628 **Table B.2 Results of the curve fitting of experimental filtration data (model solute filtration**

629 **through PAA and PES membrane) with well-established mathematical models of the**

630 **fundamental mechanisms of fouling.**

631 Curve fitting was carried out using least-square algorithm in software, OriginPro 9.0 (OriginLab

632 Corp.,USA). Parameters represent kinetic constants of the respective mechanisms, k_s (m^{-1}), k_b (s^{-1}), k_i

633 (m^{-1}) and k_c (sm^{-2} x 10^{-6}). Regression coefficient (R^2) and sum of square of the residuals (SSR) signify

634 the goodness of the fits. Standard error values for all kinetic constants were less than 5% of the value

635 of the kinetic constants. Data is represented as average values ± one standard deviation for triplicate

636 filtration runs.

Appendix C. SEM images of the fouling observed on the surface of the active layer of the 20nm

638 **PAA membranes**

<div align="center">A   B</div>

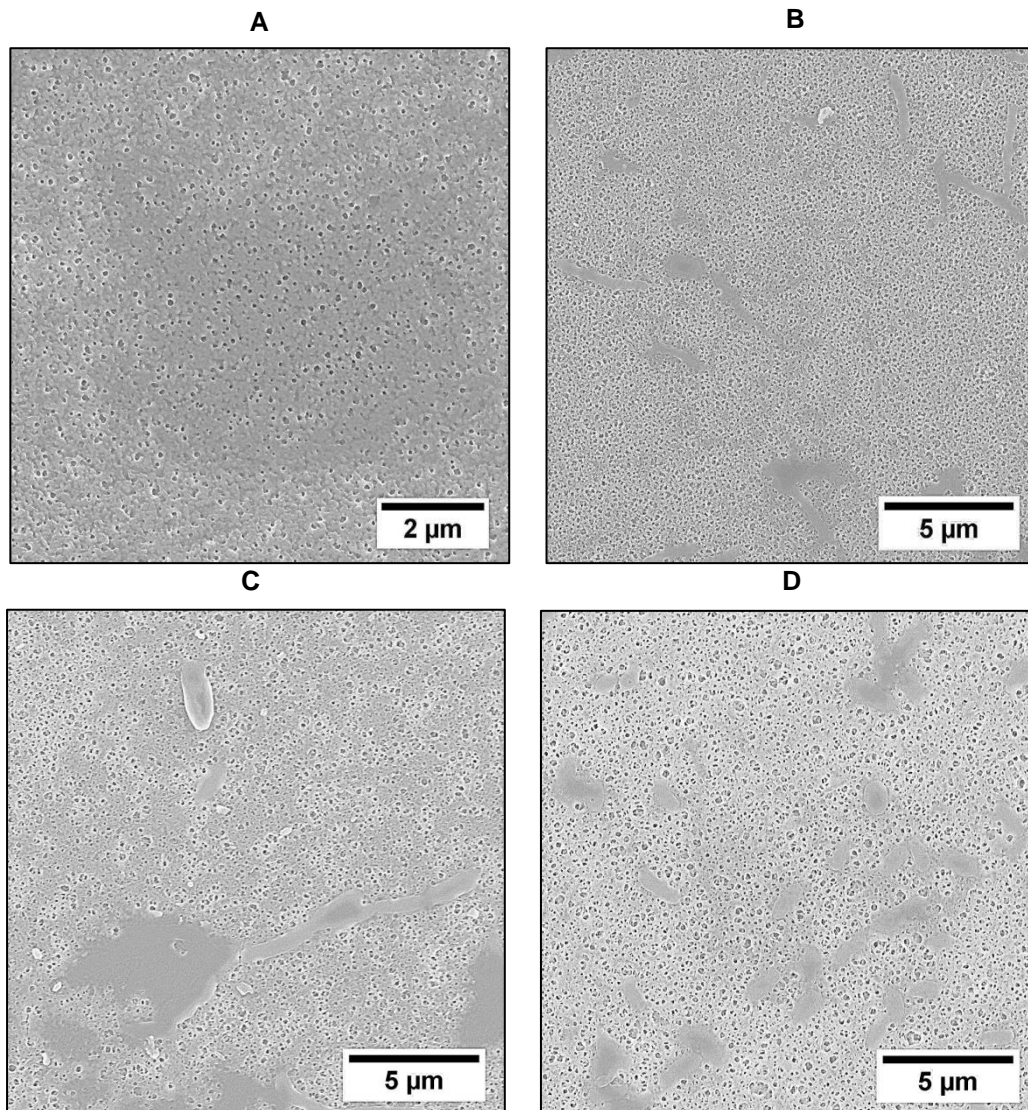<div align="center">C   D</div>
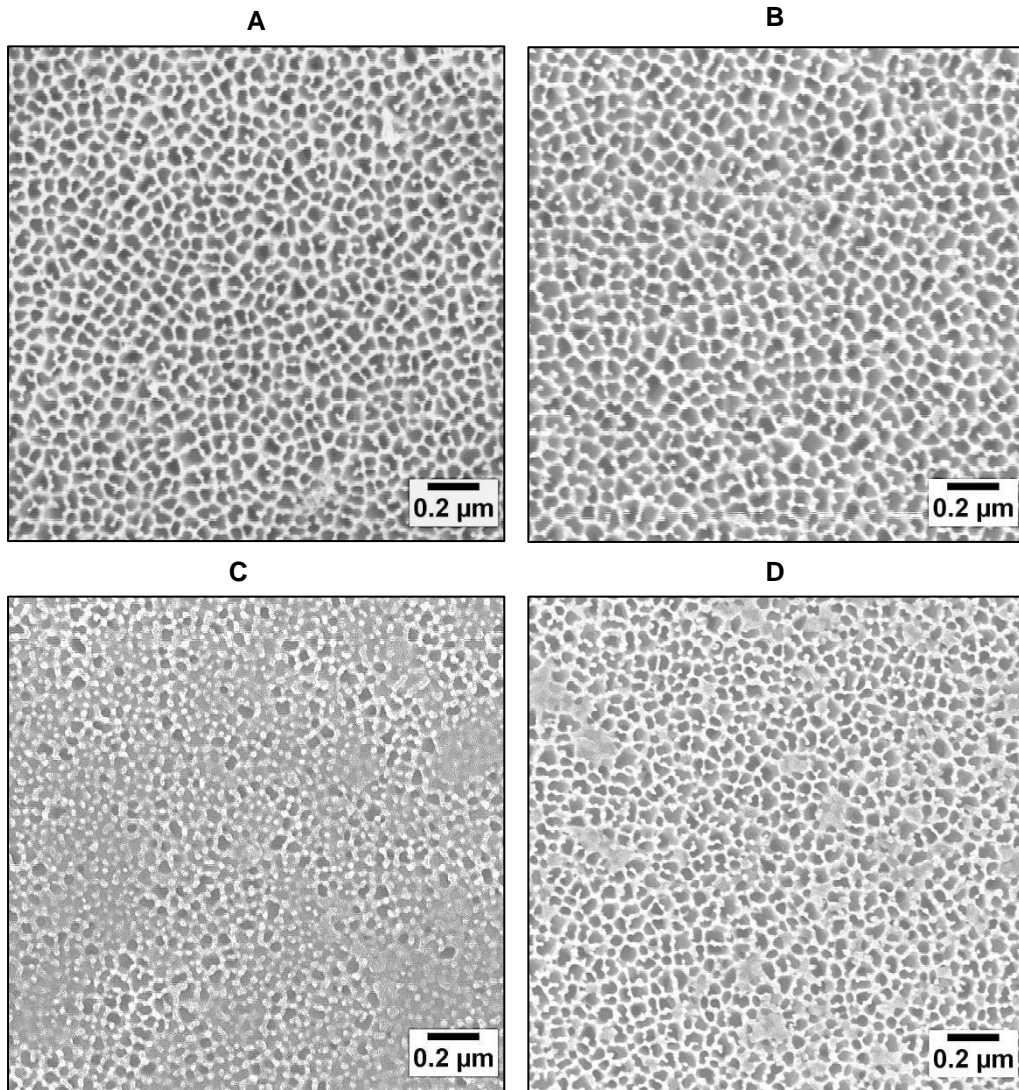
639

640 **Fig. C.1 SEM images showing fouling by different model solutes on the active layer surface of**

641 **20nm rated PAA membranes. A- Unused membrane, B- BSA fouled, C- TG fouled and D- BSA**

642 **nanoparticles fouled membrane.**

643 Scale bar represents 0.2 µm and images were taken at a magnification of 100,000 for all of the

644 samples. Images were obtained after drying and coating the membranes with uniform ultrathin (<1

645 nm) layer of platinum using sputter coater and analysed using InLens detector with less than 5kV gun

646 voltage. Field emission scanning electron microscope (Gemini Sigma, Carl Zeiss AG, Germany) was

647 used.

648 **<u>Appendix D. SEM images of the fouling observed on the surface of the active layer of the</u>**

649 **<u>300kDa PES membranes</u>**

A

B

C

D

650

651 **Fig. D.1 SEM images showing fouling by different model solutes on the active layer surface of**

652 **300kDa PES membranes. A- Unused membrane, B- BSA fouled, C- TG fouled and D- BSA**

653 **nanoparticles fouled membrane.**

654 Scale bar represents 5 μm (except A) and images were taken at a magnification of 10,000 (except

655 20,000 for A) for all of the samples. Images were obtained after drying the membranes and coating

656 with ultrathin (<1 nm) and uniform layer of platinum using sputters coater and analysed using InLens

657 detector with less than 5kV gun voltage. Field emission scanning electron microscope (Gemini Sigma,

658 Carl Zeiss AG, Germany) was used.

Appendix E. Effect of various treatments on flux recovery ratio (% of clean membrane flux) of

660 **fouled membranes after 12 diavolumes diafiltration process for fractionation of BSA and BSA**

661 **NP**
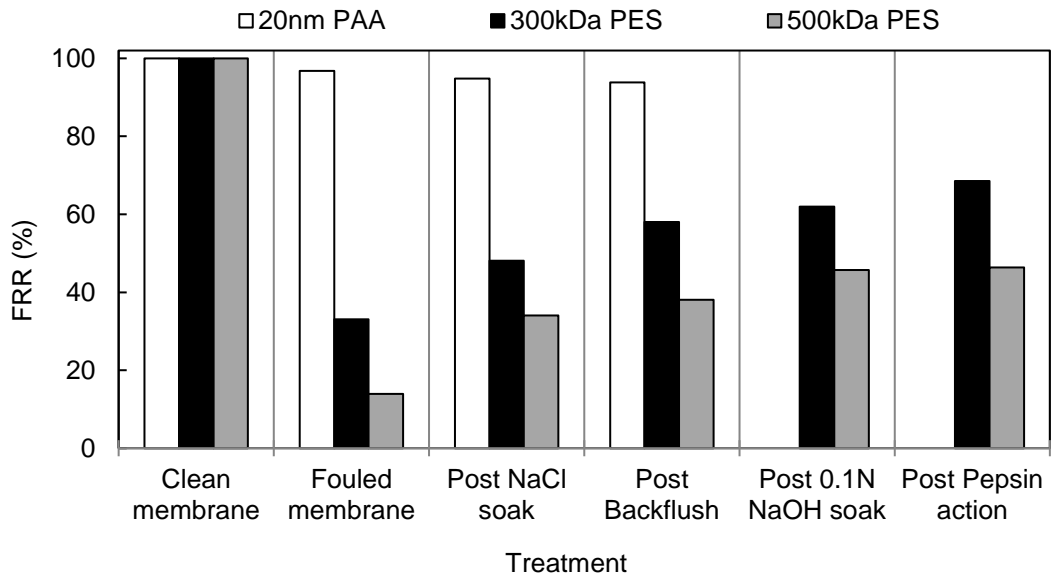
662

663 **Fig. E.1 Flux recovery ratio, FRR (% of membrane permeability for fresh membranes) for PAA**

664 **membrane and PES membranes after an extended UF/DF experiment (12 DF cycles each of**

665 **one diavolume) for fractionation of a mixture of BSA and BSA NP and effect of various**

666 **chemical treatments to remove fouling**.

667 Membranes were treated (in sequence) with 1M NaCl soak for 24 hours; buffer backflush (2 x TMP

668 used in protein filtration), 0.1 N NaOH soak for an hour and proteolytic enzyme treatment for 18 hours

669 at room temperature). PAA membrane showed ~96% of initial buffer flux recovered after rinsing with

670 buffer. Polymeric membranes could not be restored to similar levels even with the chemical

671 treatments.

APPENDIX F. Pore size distribution of the 20nm PAA and 300kDa PES membranes and overlay

673 **of particle size distribution of the model solutes**
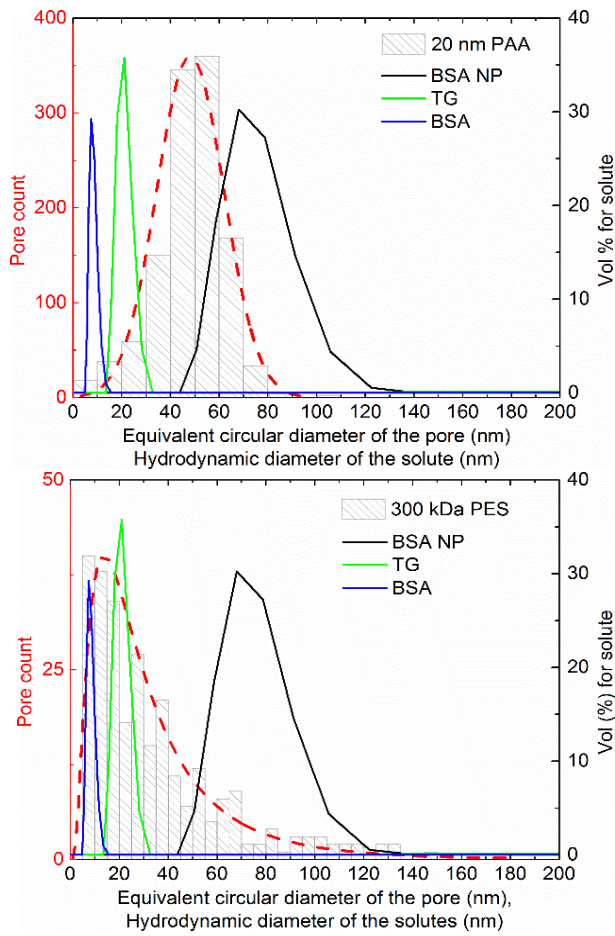
674

675 **Fig. F.1 Pore size distribution of membrane surface for 20nm PAA and 300kDa PES membrane**

676 **overlaid with particle size distribution of various solutes.**

677 **The grey bars and red dotted line represent the histogram of pore counted (Left Y-axis) upon**

678 **SEM image analysis and fitting of distribution curve respectively for membranes. Particle size**

679 **distribution of BSA NP, TG and BSA are displayed as solid lines with right side Y axis.**

680 Surface pore size in 20 nm PAA and 300kDa PES membranes followed normal and log-normal

681 distribution respectively. Larger pore sizes (>90 nm to 180 nm) were observed for the 300kDa PES

682 membrane.

References

[1] E.I. Trilisky, A.M. Lenhoff, Sorption processes in ion-exchange chromatography of viruses, J. Chromatogr. A, 1142 (2007) 2-12.

[2] M. Yu, Y. Li, S. Zhang, X. Li, Y. Yang, Y. Chen, G. Ma, Z. Su, Improving stability of virus-like particles by ion-exchange chromatographic supports with large pore size: Advantages of gigaporous media beyond enhanced binding capacity, J. Chromatogr. A, 1331 (2014) 69-79.

[3] C.S. Fernandes, B. Goncalves, M. Sousa, D.L. Martins, T. Barroso, A.S. Pina, C. Peixoto, A. Aguiar-Ricardo, A.C. Roque, Biobased monoliths for adenovirus purification, ACS Appl. Mater. Interfaces, 7 (2015) 6605-6612.

[4] Y. Wu, D. Abraham, G. Carta, Comparison of perfusion media and monoliths for protein and virus-like particle chromatography, J. Chromatogr. A, 1447 (2016) 72-81.

[5] O. Hardick, S. Dods, B. Stevens, D.G. Bracewell, Nanofiber adsorbents for high productivity downstream processing, Biotechnol. Bioeng., 110 (2013) 1119-1128.

[6] P. Nestola, D.L. Martins, C. Peixoto, S. Roederstein, T. Schleuss, P.M. Alves, J.P.B. Mota, M.J.T. Carrondo, Evaluation of novel large cut-off ultrafiltration membranes for adenovirus serotype 5 (Ad5) concentration, PLoS ONE, 9 (2014) 22.

[7] M. Weggeman, Viurs purification using ultrafiltration, in: USPTO (Ed.), Crucell Holland B.V., Leiden (NL), 2013, pp. 34.

[8] C. Peixoto, T.B. Ferreira, M.F. Sousa, M.J. Carrondo, P.M. Alves, Towards purification of adenoviral vectors based on membrane technology, Biotechnol. Prog., 24 (2008) 1290-1296.

[9] S. Subramanian, G.M. Altaras, J. Chen, B.S. Hughes, W. Zhou, N.E. Altaras, Pilot-scale adenovirus seed production through concurrent virus release and concentration by hollow fiber filtration, Biotechnol. Prog., 21 (2005) 851-859.

[10] T. Urase, K. Yamamoto, S. Ohgaki, Effect of pore structure of membranes and module configuration on virus retention, J. Membr. Sci., 115 (1996) 21-29.

[11] S. Giglia, D. Bohonak, P. Greenhalgh, A. Leahy, Measurement of pore size distribution and prediction of membrane filter virus retention using liquid–liquid porometry, J. Membr. Sci., 476 (2015) 399-409.

[12] J.J. Deng, C.S. Toh, Impedimetric DNA Biosensor Based on a Nanoporous Alumina Membrane for the Detection of the Specific Oligonucleotide Sequence of Dengue Virus, Sensors, 13 (2013) 7774-7785.

[13] C.C. Chen, Z.L. Lai, G.J. Wang, C.Y. Wu, Polymerase chain reaction-free detection of hepatitis B virus DNA using a nanostructured impedance biosensor, Biosens Bioelectron, 77 (2016) 603-608.

[14] P. Chaturvedi, S.D. Rodriguez, I. Vlassiouk, I.A. Hansen, S.N. Smirnov, Simple and Versatile Detection of Viruses Using Anodized Alumina Membranes, ACS Sens, 1 (2016) 488-492.

[15] A.C. Attaluri, Z. Huang, A. Belwalkar, W. Van Geertruyden, D. Gao, W. Misiolek, Evaluation of nano-porous alumina membranes for hemodialysis application, ASAIO J, 55 (2009) 217-223.

[16] H.U. Osmanbeyoglu, T.B. Hur, H.K. Kim, Thin alumina nanoporous membranes for similar size biomolecule separation, J. Membr. Sci., 343 (2009) 1-6.

[17] T. Yamashita, S. Kodama, T. Kemmei, M. Ohto, E. Nakayama, T. Muramoto, A. Yamaguchi, N. Teramae, N. Takayanagi, Separation of adenine, adenosine-5'-monophosphate and adenosine-5'-triphosphate by fluidic chip with nanometre-order diameter columns inside porous anodic alumina using an aqueous mobile phase, Lab Chip, 9 (2009) 1337-1339.

[18] K.P. Lee, D. Mattia, Monolithic nanoporous alumina membranes for ultrafiltration applications: Characterization, selectivity-permeability analysis and fouling studies, J. Membr. Sci., 435 (2013) 52-61.

[19] P. Prádanos, A. Hernández, J.I. Calvo, F. Tejerina, Mechanisms of protein fouling in cross-flow UF through an asymmetric inorganic membrane, J. Membr. Sci., 114 (1996) 115-126.

[20] P. Pradanos, J.I. Arribas, A. Hernandez, Retention of Proteins in Cross-Flow Uf through Asymmetric Inorganic Membranes, AIChE J., 40 (1994) 1901-1910.

[21] J.M. Moon, D. Akin, Y. Xuan, P.D. Ye, P.X. Guo, R. Bashir, Capture and alignment of phi29 viral particles in sub-40 nanometer porous alumina membranes, Biomed. Microdevices, 11 (2009) 135-142.

[22] G. Jeon, M. Jee, S.Y. Yang, B.Y. Lee, S.K. Jang, J.K. Kim, Hierarchically Self-Organized Monolithic Nanoporous Membrane for Excellent Virus Enrichment, ACS Appl. Mater. Interfaces, 6 (2014) 1200-1206.

[23] G.M.F. Braas, S.G. Walker, A. Lyddiatt, Recovery in aqueous two-phase systems of nanoparticulates applied as surrogate mimics for viral gene therapy vectors, J. Chromatogr. B, 743 (2000) 409-419.

742 [24] S. Joseph, L. Wenger, D. Bracewell, O. Thomas, Manufacture and characterisation of protein
743 nanoparticles as surrogate virus and VLP mimetics for the optimisation of chromatography media,
744 New Biotechnol., 33 (2016) S115.
745 [25] B. Storp, A. Engel, A. Boeker, M. Ploeger, K. Langer, Albumin nanoparticles with predictable size
746 by desolvation procedure, J. Microencapsul., 29 (2012) 138-146.
747 [26] M. Jin, N. Szapiel, J. Zhang, J. Hickey, S. Ghose, Profiling of host cell proteins by two-
748 dimensional difference gel electrophoresis (2D-DIGE): Implications for downstream process
749 development, Biotechnol. Bioeng., 105 (2010) 306-316.
750 [27] G. Bolton, D. LaCasse, R. Kuriyel, Combined models of membrane fouling: Development and
751 application to microfiltration and ultrafiltration of biological fluids, J. Membr. Sci., 277 (2006) 75-84.
752 [28] P. Mulherkar, R. van Reis, Flex test: a fluorescent dextran test for UF membrane
753 characterization, J. Membr. Sci., 236 (2004) 171-182.
754 [29] B.L. Cheang, A.L. Zydney, A two-stage ultrafiltration process for fractionation of whey protein
755 isolate, J. Membr. Sci., 231 (2004) 159-167.
756 [30] E. Burova, E. Loffe, Chromatooraphic purification of recombinant adenoviral and adeno-
757 associated viral vectors: methods and implications, Gene Therapy, 12 (2005) S5-S17.
758 [31] M. Bakhshayeshi, D.M. Kanani, A. Mehta, R. van Reis, R. Kuriyel, N. Jackson, A.L. Zydney,
759 Dextran sieving test for characterization of virus filtration membranes, J. Membr. Sci., 379 (2011) 239-
760 248.
761 [32] A.L. Zydney, A. Xenopoulos, Improving dextran tests for ultrafiltration membranes: Effect of
762 device format, J. Membr. Sci., 291 (2007) 180-190.
763 [33] H. Lutz, Ultrafiltration for Bioprocessing, 1st ed., Woodhead Publishing, Cambridge,UK, 2015.
764 [34] M.C. Porter, Concentration Polarization with Membrane Ultrafiltration, Ind. Eng. Chem. Prod.
765 Res. Dev., 11 (1972) 234-248.
766 [35] V.G.J. Rodgers, R.E. Sparks, Effect of transmembrane pressure pulsing on concentration
767 polarization, J. Membr. Sci., 68 (1992) 149-168.
768 [36] A. Tandon, S.K. Gupta, G.P. Agarwal, Modelling of protein transmission through ultrafiltration
769 membranes, J. Membr. Sci., 97 (1994) 83-90.

770